Journal of
Applied
Crystallography

ISSN 0021-8898

Received 16 July 2009
Accepted 1 October 2009

© 2009 International Union of Crystallography
Printed in Singapore – all rights reserved

Scherrer grain-size analysis adapted to grazing-incidence scattering with area detectors

Detlef-M. Smilgies

Cornell High Energy Synchrotron Source (CHESS), Cornell University, Ithaca, NY 14853, USA. Correspondence e-mail: dms79@cornell.edu

Ever since its formulation, the Scherrer formula has been the workhorse for quantifying finite size effects in X-ray scattering. Various aspects of Scherrer-type grain-size analysis are discussed with regard to the characterization of thin films with grazing-incidence scattering methods utilizing area detectors. After a brief review of the basic features of Scherrer analysis, a description of resolution-limiting factors in grazing-incidence scattering geometry is provided. As an application, the CHESS D1 beamline is characterized for typical scattering modes covering length scales from the molecular scale to the nanoscale.

1. Introduction

The ubiquitous Scherrer (1918) formula is, apart from Bragg's law, probably the most referred to formula in X-ray science. The Scherrer formula relates the breadth B_{hkl}, or full width at half-maximum, of a diffraction spot (hkl) to the average grain size D_{hkl} in the material under study:

$$D_{hkl} = \frac{K\lambda}{B_{hkl}\cos(\theta_{hkl})}, \qquad (1)$$

where λ is the X-ray wavelength and θ_{hkl} is the Bragg angle. The Scherrer constant K is most often cited in the literature as having a value of about 0.9, as derived in Scherrer's original paper with $K = 2[2\ln(2)/\pi]^{1/2} \simeq 0.93$ (see Warren, 1969).

We obtain a more modern representation in reciprocal space rather than angular space, when we realize that

$$\Delta q_{hkl} = \frac{4\pi}{\lambda}\cos(\theta_{hkl})\frac{B_{hkl}}{2}, \qquad (2)$$

where we identified the breadth $B_{hkl} = \Delta(2\theta_{hkl})$ with the width of the Bragg spot with regard to scattering angle and obtain

$$D_{hkl} = 2\pi K/\Delta q_{hkl}. \qquad (3)$$

Finally, another useful parameter is the average number of Bragg planes,

$$\overline{N}_{hkl} = D_{hkl}/d_{hkl} = q_{hkl}/\Delta q_{hkl}, \qquad (4)$$

where q_{hkl} and d_{hkl} are the scattering vector and the d spacing associated with Bragg reflection (hkl), respectively. $\overline{N}_{hkl}$ is independent of the chosen representation in real or reciprocal space and is an intuitive quantity to describe poorly ordered systems.

2. Patterson analysis of the Scherrer constant

Patterson (1949*a*,*b*) introduced a more general approach to describe finite grain sizes by introducing a shape function $f(\mathbf{r})$, which has the value of 1 inside the shape and 0 elsewhere. The product of the shape function and the infinite lattice yields a finite crystal with a shape given by the shape function. Applying the convolution theorem, the intensity distribution for a reflection of a finite crystal is then given by the convolution of the delta functions at the reciprocal-lattice points and the Fourier transform $F(\mathbf{q})$ of the shape function. Thus $|F(\mathbf{q})|^2$ defines the shape and width of the diffraction spot. We note that Patterson's $F(\mathbf{q})$ is identical to the form factors of objects with a constant electron density that are extensively used in small-angle scattering (Guinier & Fournet, 1955; Guinier, 1963; Glatter & Kratky, 1982; for recent reviews see Pedersen, 1997; Lazzari, 2002; Förster *et al.*, 2005).

Two types of grain shapes seem to be prevalent: more or less spherical and cylindrical. For a spherical grain with radius R, the form factor is given as

$$F(q) = \frac{4}{3}\pi R^3\left[3\frac{\sin(qR) - qR\cos(qR)}{(qR)^3}\right]. \qquad (5)$$

The form factor is normalized, so that $F(0)$ equals the volume of a single sphere (Lazzari, 2002). Comparing the breadth of $|F(q)|^2$ to the characteristic grain dimension $2R$ according to equation (3) results in a K value of 1.123.

The form factor of a cylinder of height H and radius R is given by

$$F(q) = 2\pi R^2 H\left[\frac{2J_1(q_{||}R)}{q_{||}R}\right]\left[\frac{\sin(q_z H/2)}{q_z H/2}\right] \qquad (6)$$

(Lazzari, 2002). $J_1(x)$ is the first-order Bessel function; q_z and $q_{||}$ are the q components parallel and perpendicular to the cylinder axis, respectively. Most interesting are the limiting cases $R >> H$ and $H >> R$. In the first case, we have a plate-like habit of the ordered grains, in the second one a needle-like habit. If we assume that the large dimension is beyond the

resolution limit in both cases, we obtain the following K numbers:

(1) Platelets: we obtain the thickness H from reflections perpendicular to the plane. Breadth analysis yields the factor K = 0.886 (Guinier, 1963), close to Scherrer's original result. This case is also interesting for lamellar systems and describes the average lamellar stack height.

(2) Needles: we obtain the thickness $2R$ from reflections perpendicular to the needle axis. Breadth analysis yields K = 1.000. This case includes hexagonally packed cylindrical phases in block copolymers and surfactant mesophases; it is also relevant for equatorial reflections in fibers.

The three cases discussed, spherical, plate-like and rod-like, are the most important ones for hard and soft materials with limited order, where only a limited number of reflections are available. Further values for K are obtained when other shapes or the grain-size distributions are included (see reviews by Langford & Wilson, 1978; Scardi & Leoni, 2001). In all cases K remains on the order of 1.

3. Other contributions to the breadth

It has to be emphasized that a radial scan is needed in order to determine the breadth $B_{\rm exp}$ and the associated grain size accurately. For area-detector data this means that breadth should be determined in the radial direction starting from the direct-beam position. In grazing-incidence scattering close to the critical angles, certain scattering features are due to the scattering of the reflected beam (Lee *et al.*, 2005; Busch *et al.*, 2006), and thus the radial direction is determined with respect to the location of the specularly reflected beam. In contrast, tangential scans, or scanning directions with both radial and tangential components, are prone to additional broadening due to the sample orientation distribution function, also referred to as mosaicity or texture. Hence, tangential breadths are always larger than radial ones, and the use of non-radial breadths may result in underestimation of the grain size.

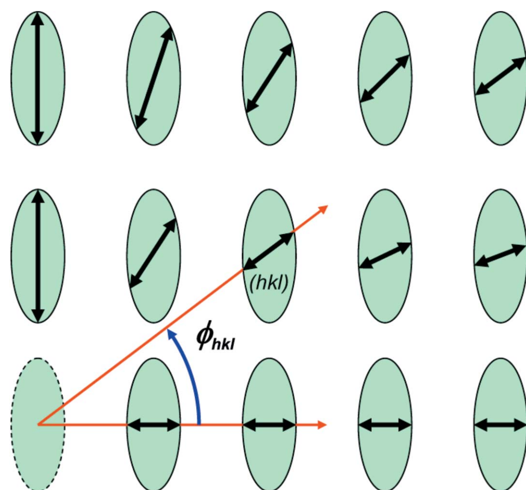

Figure 1
Anisotropic spot breadth indicating an anisotropic grain size, for instance in thin-film samples where the film thickness limits the vertical grain size. The detector azimuth φ_{khl}, *i.e.* the angle of the line extending from the direct-beam mark to a specific reflection with the horizontal plane, is marked for a sample reflection (*hkl*). If only a part of the breadths can be measured in radial scans owing to weak scattering intensities, the horizontal and the vertical breadth and the associated grain sizes can still be reconstructed (see text).

A special case deviating from this general rule is systems with pronounced preferential order induced by the substrate surface, as often seen in surface scattering and thin-film studies. If the scattering features have a rod-like appearance, with the rods extending perpendicular to the substrate, widths measured along the rods should be a good indicator of the grain size perpendicular to the substrate. This case is particularly interesting for thin films where the lateral grain size can often be assumed to be isotropic, while the vertical grain size can be limited by the film thickness. In fact, it is generally of great interest to compare vertical grain size and film thickness (see, for example, Papadakis *et al.*, 2008).

However, if the scattering rods are smeared out into arcs as a result of film mosaicity, it is safest to resort to the radial widths for grain-size analysis and then extrapolate to the vertical grain size by comparing reflections at different azimuth angles. In the case of organic thin films, often only a few reflections are intense enough to be used for breadth determination, which often do not fall along the radial direction of interest. In the following, we provide a simple method of obtaining the relevant average grain dimensions in such a case.

Fig. 1 shows the intrinsic widths for an array of diffraction spots, where it is assumed that only the radial breadths can be measured reliably. Assuming an ellipsoidal shape of the thin-film grains, the breadth ellipsoid can be reconstructed by measuring the radial breadth of all reasonably intense reflections as well as their detector azimuths φ_{hkl}, and then fitting the horizontal and vertical grain sizes $B_{\rm H}$ and $B_{\rm V}$. The equation of the breadth ellipse can be found as

$$\frac{\left[B_{hkl}\cos(\varphi_{hkl})\right]^2}{B_{\rm H}^2}+\frac{\left[B_{hkl}\sin(\varphi_{hkl})\right]^2}{B_{\rm V}^2}=1 \qquad (7a)$$

where B_{hkl} and φ_{hkl} correspond to polar coordinates of the breadth ellipsoid (see Fig. 1). This *Ansatz* yields immediately

$$B_{hkl}(\varphi_{hkl})=\frac{1}{\{[\cos^2(\varphi_{hkl})/B_{\rm H}^2]+[\sin^2(\varphi_{hkl})/B_{\rm V}^2]\}^{1/2}}. \qquad (7b)$$

In addition to the proper measurement of breadths discussed above, other intrinsic sample properties can contribute to the radial breadths. Strain fields and/or short-range ordering can lead to additional line broadening of the higher-order reflections. In principle, such effects have to be separated from the finite size effect by careful spot-breadth analysis as a function of the scattering angle; see Williamson & Hall (1953) for strain fields or Hosemann & Bagchi (1962) for analysis of short-range order.

Strain effects are most pronounced in hard-matter thin films and deposits. Soft materials such as polymers, liquid crystals or nanoparticle supracrystals are relatively compliant and often rather deform, *i.e.* create grain boundaries or defects, than

build up extended strain fields. Often soft materials may not show true long-range order and, hence, may only display a few diffraction orders. In both cases, the breadth of the lowest-order reflections, where such additional broadening effects are the least pronounced, will still provide valuable information on the average grain size.

4. Resolution analysis

Apart from sample-specific contributions to the peak breadth, it is important that the resolution $B_{\rm res}$ of the apparatus is accurately determined and accounted for:

$$B_{hkl} = (B_{\rm exp}^2 - B_{\rm res}^2)^{1/2}, \quad (8)$$

where $B_{\rm exp}$ denotes the experimentally determined breadth from a radial scan.

$B_{\rm res}$ shall be examined here for the case of grazing-incidence small- and wide-angle scattering (GISAXS/GIWAXS). These techniques constitute powerful methods to characterize the structure of thin films on the molecular scale (GIWAXS) and on the nanoscale (GISAXS), and have been extensively used for the study of soft and hard materials on surfaces or in thin films (Levine *et al.*, 1989; Sirringhaus *et al.*, 1999; Smilgies *et al.*, 2002; Lazzari, 2002; Renaud *et al.*, 2003; Lee *et al.*, 2005; Busch *et al.*, 2006; Breiby *et al.*, 2008). In either case, the X-ray beam impinges on the surface under grazing incidence close to the critical angle of the film and the scattered photons are collected with an area detector such as a CCD camera or an image plate.

Another powerful surface scattering technique is grazing-incidence diffraction (GID). Although the limits between GIWAXS and GID are somewhat fluid, in the following it will be understood that GIWAXS measurements are primarily concerned with collecting diffuse scattering with an area detector, while in GID typically higher-resolution scans using point or line detectors are performed, in conjunction with collimating slits or Soller collimators (see, for instance, Smilgies *et al.*, 2005). The use of collimation significantly changes the resolution function and has been discussed by Robach *et al.* (2000) and Jedrecy (2000). In the following, we will be concerned with the GIWAXS case, which follows the same considerations as apply for GISAXS.

Principal contributions to the scattering resolution are the horizontal and vertical beam divergences $\sigma'_{\rm H}$ and $\sigma'_{\rm V}$, and the beam-energy bandwidth η, using phase-space notation (Smilgies, 2008). The beam divergence in both principal directions can be estimated from the horizontal and vertical source sizes, $\sigma_{\rm H}$, $\sigma_{\rm V}$, and the distance of the sample from the source. The energy bandwidth can be determined from the optical properties of the monochromator.

Assuming an elliptical beam profile with main axes $\sigma'_{\rm H}$ and $\sigma'_{\rm V}$, the beam divergence in the radial direction for a given detector azimuth angle φ is given as

$$\sigma'_{\rm R}(\varphi) = \frac{1}{\{[\cos^2(\varphi)/\sigma'^2_{\rm H}] + [\sin^2(\varphi)/\sigma'^2_{\rm V}]\}^{1/2}} \quad (9)$$

using the method to derive equation (7*b*). The divergence of the scattered beam is

$$B_{\rm div} = \sigma'_{\rm R}, \quad (10)$$

where we assume that the whole incident radiation fan is Bragg reflected owing to the mosaicity of the sample. This assumption is usually satisfied in soft materials as well as in hard-material deposits with finite mosaicity.

The radial divergence is increased by the energy bandwidth according to

$$B_{\rm BW} = 2\eta \tan(2\theta_{hkl}/2). \quad (11)$$

For Si(111) optics with $\eta = 10^{-4}$, this smearing can usually be neglected; however, for multilayer optics with η in the range 0.5–2% (Kazimirov *et al.*, 2006), it definitely has to be taken into account.

An effect peculiar to grazing-incidence scattering is geometric smearing, as illustrated in Fig. 2. The cause is the finite length of the footprint of the beam on the sample (Yang, 2005). For typical grazing angles between 0.1 and 0.3° and 0.1 mm beam height, any sample shorter than 40 mm along the beam gets fully illuminated. Hence, the resolution is affected by the width w of the footprint of the beam on the sample. If every volume element within the illuminated streak scatters, all intensity under the scattering angle 2θ is spread out into a radial streak on the detector of width w' with

$$w' = w \tan(2\theta) \quad (12)$$

and thus the geometric smearing is given by

$$B_{\rm geo} = [w \tan(2\theta)]/L, \quad (13)$$

where L is the distance from sample to detector.

The geometric smearing effect is most pronounced at large scattering angles (GIWAXS), while for small-angle scattering ($2\theta < 1°$) it becomes small.

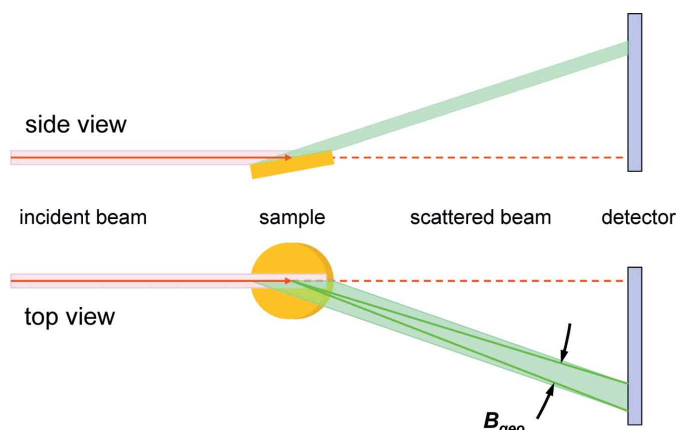

Figure 2
Schematic depiction of the geometric smearing effect as a result of the finite sample size (lengths and angles are not to scale). A side view and a top view are provided for an in-plane reflection ($\varphi_{hkl} \simeq 0$). In grazing-incidence geometry, typically the full length of the sample is illuminated. For an arbitrary detector azimuth, the smearing occurs in the radial direction.

In all, there are three contributions to the radial resolution: the beam divergence, the beam bandwidth and the geometric smearing. The combined resolution can be written as

$$B_{\rm res}(2\theta, \varphi) = [B_{\rm div}(\varphi)^2 + B_{\rm BW}(\eta, 2\theta)^2 + B_{\rm geo}(w, 2\theta)^2]^{1/2} \quad (14)$$

or, in terms of scattering vector resolution,

$$\Delta q_{\rm res} = \frac{4\pi}{\lambda} \cos\left(\frac{2\theta_{hkl}}{2}\right) \frac{B_{\rm res}}{2}. \quad (15)$$

For practical purposes, the resolution limit of the apparatus is reached if $B_{\rm exp}$ does not exceed $B_{\rm res}$ by at least 50%. If the Scherrer formula is applied to $B_{\rm res}$, we can determine the resolution limit of the apparatus in real space, $D_{\rm lim}$, which can serve as a lower limit for the actual grain size.

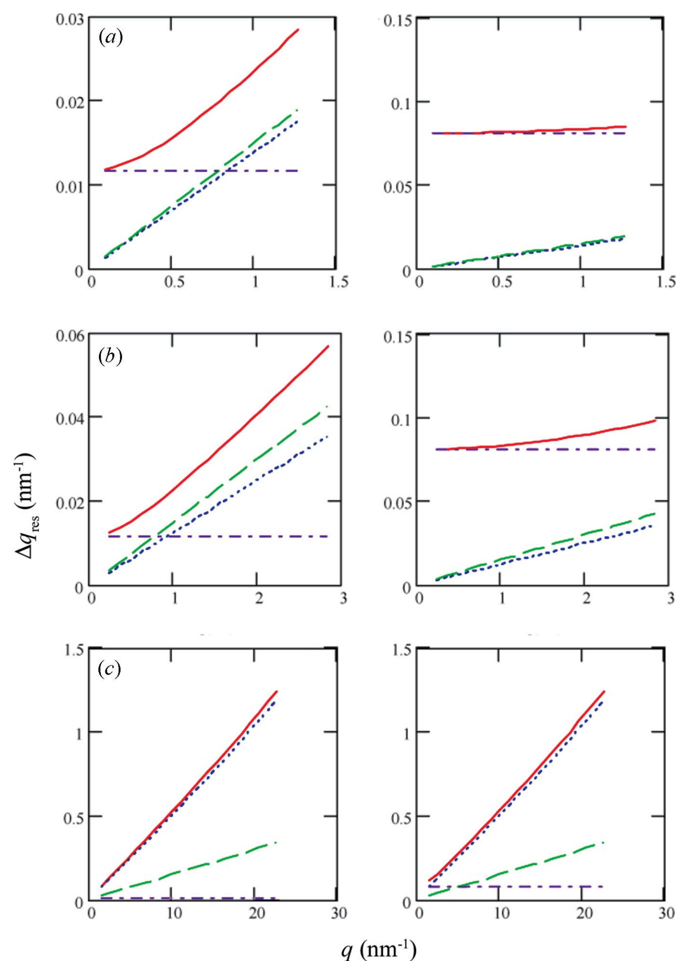

Figure 3
Resolution limits for typical D1 setups: (*a*) GISAXS-I, (*b*) GISAXS-II and (*c*) GIWAXS. The left and right columns display the resolution in the horizontal and vertical directions, respectively. For a description of experimental parameters see text. The total scattering resolution (solid line) is plotted along with the partial contributions from geometric smearing (dotted line), bandwidth smearing (dashed line) and beam divergence (dash–dotted line) over the q range covered by the detector.

5. Application

GISAXS and GIWAXS beamlines come in many flavors and are often based on pre-existing equipment, such as SAXS pinhole cameras, reflectometers or surface diffractometers. The same applies to neutron scattering instruments. The above description of the resolution captures the important aspects; however, a specific analysis will have to be done for each individual setup.

As an application example, we will consider station D1 at the Cornell High Energy Synchrotron Source (CHESS). D1 is supplied with an X-ray beam from a hard-bent dipole magnet in the 5.2 GeV CESR storage ring at Cornell University. Horizontal and vertical source sizes are $\sigma_{\rm H} = 2$ mm and $\sigma_{\rm V} = 1$ mm, using phase-space notation (Matsushita & Kaminaga, 1980*a*,*b*; Smilgies, 2008). Two 30 Å period Mo:B_4C synthetic multilayers are used in a vertical double-bounce monochromator. A slit system collimates the beam for grazing-incidence experiments to 0.5 (H) × 0.1 mm (V). The sample is at about 13 m from the source point, and sample-to-detector distances vary between 100 (GIWAXS) and 500–1800 mm (GISAXS). Scattered photons are detected with a CCD-type area detector (MedOptics) with a pixel size of 47 µm and an aperture of 48 × 48 mm.

The horizontal divergence $\sigma'_{\rm H}$ can be estimated from the horizontal source size and the distance of the sample from the source as 0.16 mrad. Energy analysis by measuring the position and breadth of the (111) and (333) reflections of an Si(111) single crystal in the vertical plane yields a vertical beam divergence $\sigma'_{\rm V}$ of 1.6 mrad and an energy bandwidth $\eta = \Delta E/E = \Delta\lambda/\lambda$ of 1.5% (Shastri, 1995). Hence, the measured $\sigma'_{\rm V}$ is significantly larger than the expected value of 0.08 mrad from the source size (1 mm) and distance (13 m) and dominated by multilayer properties.

With the parameters described above, D1 is optimized to collect weak, diffuse scattering intensities from relatively poorly ordered systems at medium resolution (up to 200 nm), as is typical for thin films of nanostructured soft materials, where the amount of flux on the sample is often the limiting factor. As an application, we will calculate the q resolution for typical D1 experimental setups: (*a*) GISAXS-I (block copolymers, nanocomposites), (*b*) GISAXS-II (nanoparticle superlattices, nanoporous materials) and (*c*) GIWAXS (semicrystalline polymers, aromatic molecules).

The maximum scattering angle is given by the size of the area detector and its distance from the sample. The MedOptics detector at CHESS D1 has an effective active area of 45 × 45 mm, if edge effects are to be avoided. Typical distances are 1800 (GISAXS-I), 800 (GISAXS-II) and 100 mm (GIWAXS). The minimum scattering angle is limited by the size of the beamstop (typically 3 mm for GISAXS and 1.5 mm for GIWAXS) as well as its location relative to the sample (1650 and 650 mm for GISAXS-I and II, respectively, and 50 mm for GIWAXS).

Fig. 3 presents both horizontal (left column) and vertical (right column) resolution values for the three setups. Using equation (14), we switched to a more modern representation

in reciprocal space, and we analysed the various contributions from equation (13) to the overall resolution Δq_{res}. We see that in the GIWAXS case the grain-size resolution is strongly limited by the geometric smearing, reaching about 5% of the q value. Because of this limitation, it is important to keep the sample width w below 5 mm for GIWAXS, which at a 100 mm sample–detector distance still amounts to a 5% effect. Nonetheless, useful information can still be obtained at the smaller scattering vectors, for instance for lamellar peaks in semicrystalline polymers (see, for example, Huang *et al.*, 2009). Moreover, GIWAXS is a very convenient technique for time-resolved studies or scanning studies of inhomogeneous thin films, capturing all relevant information in a single image, with a time resolution of 5–10 s per frame at D1, as given by the available X-ray flux onto the sample and the read-out time of the area detector.

From the formulae assembled above, we can determine that, in order to match the geometric smearing to the bandwidth smearing, the active scattering area would have to be reduced to 2 mm. Confining the beam footprint by working with small strips of material on a typical wafer sample of 5–10 mm width or using vertical focusing (Yang, 2005) have both been employed to improve the GIWAXS spot resolution, while still maintaining the ability to line up the sample in the beam.

In the GISAXS case, contributions are more balanced. The larger vertical beam divergence due to the multilayer monochromator limits the achievable vertical resolution. However, the vertical resolution requirements for thin films are relaxed, because the film thickness sets a natural limit on the maximum grain-size resolution needed. The best grain-size resolution is achieved in the horizontal direction, with a figure of merit of $q/\Delta q$ of 40 which amounts to micrometre-sized grains considering the typical d spacings of 20–50 nm probed in this mode. Overall, our calculation shows clearly that the resolution correction is essential in order to obtain reliable estimates of the size of ordered regions in the thin-film samples studied.

The author has greatly benefitted from discussions with Lin Yang, National Synchrotron Light Source, and John Nagle, Carnegie–Mellon University, as well as with the general D1 user community. Don Bilderback (CHESS) is thanked for commenting on the manuscript. This work is based upon research conducted at the Cornell High Energy Synchrotron Source (CHESS) which is supported by the National Science Foundation and the National Institutes of Health/National Institute of General Medical Sciences under NSF award No. DMR-0225180.

References

Breiby, D. W., Bunk, O., Andreasen, J. W., Lemke, H. T. & Nielsen, M. M. (2008). *J. Appl. Cryst.* **41**, 262–271.
Busch, P., Rauscher, M., Smilgies, D.-M., Posselt, D. & Papadakis, C. M. (2006). *J. Appl. Cryst.* **39**, 433–442.
Förster, S., Timmann, A., Konrad, M., Schellbach, C., Meyer, A., Funari, S. S., Mulvaney, P. & Knott, R. J. (2005). *Phys. Chem. B*, **109**, 1347–1360.
Glatter, O. & Kratky, O. (1982). Editors. *Small-Angle X-ray Scattering*. London: Academic Press.
Guinier, A. (1963). *X-ray Diffraction in Crystals, Imperfect Crystals, and Amorphous Bodies.* San Francisco: WH Freeman.
Guinier, A. & Fournet, G. (1955). *Small Angle Scattering of X-rays.* New York: Wiley.
Hosemann, R. & Bagchi, S. N. (1962). *Direct Analysis of Diffraction by Matter.* Amsterdam: North-Holland.
Huang, Y.-F., Chang, C.-W., Smilgies, D.-M., Jeng, U.-S., Inigo, A. R., White, J. D., Li, K.-C., Lim, T.-S., Li, T.-D., Chen, H.-Y., Chen, S.-A., Chen, W.-C. & Fann, W.-S. (2009). *Adv. Mater.* **21**, 1–5.
Jedrecy, N. (2000). *J. Appl. Cryst.* **33**, 1365–1375.
Kazimirov, A., Smilgies, D.-M., Shen, Q., Xiao, X., Hao, Q., Fontes, E., Bilderback, D. H., Gruner, S. M., Platonov, Y. & Martynov, V. V. (2006). *J. Synchrotron Rad.* **13**, 204–210.
Langford, J. I. & Wilson, A. J. C. (1978). *J. Appl. Cryst.* **11**, 102–113.
Lazzari, R. (2002). *J. Appl. Cryst.* **35**, 406–421.
Lee, B., Park, I., Yoon, J., Park, S., Kim, J., Kim, K.-W., Chang, T. & Ree, M. (2005). *Macromolecules*, **38**, 4311–4323.
Levine, J. R., Cohen, J. B., Chung, Y. W. & Georgopoulos, P. (1989). *J. Appl. Cryst.* **22**, 528–532.
Matsushita, T. & Kaminaga, U. (1980*a*). *J. Appl. Cryst.* **13**, 465–471.
Matsushita, T. & Kaminaga, U. (1980*b*). *J. Appl. Cryst.* **13**, 472–478.
Papadakis, C. M., Di, Z., Posselt, D. & Smilgies, D.-M. (2008). *Langmuir*, **24**, 13815–13818.
Patterson, A. L. (1949*a*). *Phys. Rev.* **56**, 972–977.
Patterson, A. L. (1949*b*). *Phys. Rev.* **56**, 978–982.
Pedersen, J. S. (1997). *Adv. Colloid Interface Sci.* **70**, 171–210.
Renaud, G., Lazzari, R., Revenant, C., Barbier, A., Noblet, M., Ulrich, O., Leroy, F., Jupille, J., Borensztein, Y., Henry, C. R., Deville, J.-P., Scheurer, F., Mane-Mane, J. & Fruchart, O. (2003). *Science*, **300**, 1416–1419.
Robach, O., Garreau, Y., Aïd, K. & Véron-Jolliot, M. B. (2000). *J. Appl. Cryst.* **33**, 1006–1018.
Scardi, P. & Leoni, M. (2001). *Acta Cryst.* A**57**, 604–613.
Scherrer, P. (1918). *Nachr. Ges. Wiss. Göttingen*, **26**, 98–100.
Shastri, S. (1995). CHESS Technical Memorandum. Available as web resource *via* http://www.chess.cornell.edu/misc/xrclcena.htm.
Sirringhaus, H., Brown, P. J., Friend, R. H., Nielsen, M. M., Bechgaard, K., Langeveld-Voss, B. M. W., Spiering, A. J. H., Janssen, R. A. J., Meijer, E. W., Herwig, P. & de Leeuw, D. M. (1999). *Nature* (*London*), **401**, 685–688.
Smilgies, D.-M. (2008). *Appl. Opt.* **47**, E106–E115.
Smilgies, D.-M., Blasini, D. R., Hotta, S. & Yanagi, H. (2005). *J. Synchrotron Rad.* **12**, 807–811.
Smilgies, D.-M., Busch, P., Posselt, D. & Papadakis, C. M. (2002). *Synchrotron Radiat. News*, **15**, 35–41.
Warren, B. E. (1969). *X-ray Diffraction.* Reading: Addison-Wesley.
Williamson, G. K. & Hall, W. H. (1953). *Acta Metall.* **1**, 22–31.
Yang, L. (2005). *Macromol. Res.* (*Polym. Soc. Korea*), **13**, 538–541.